PAPER

CrossMark
click for updates

Nanocasting synthesis of mesoporous SnO$_2$ with a tunable ferromagnetic response through Ni loading†

Junpeng Fan,[a] Jin Zhang,[a] Pau Solsona,[a] Santiago Suriñach,[a] Maria Dolors Baró,[a] Jordi Sort[ab] and Eva Pellicer*[a]

Undoped and Ni-doped ordered mesoporous SnO$_2$ powders ([Ni(II)]/[Sn(II)] = 0 : 100, 5 : 95, 15 : 85, 20 : 80) were synthesized by nanocasting from mesoporous KIT-6 silica. The resulting Ni content in the Ni-loaded powders ranged between 1 at% and 9 at%. Successful replication of the silica template was verified by scanning electron microscopies for all samples. Residual silicon content did not surpass 4 at%. X-ray diffraction analyses showed that the powders were nanocrystalline, being the rutile-like phase of SnO$_2$ the dominant structure. Changes in the lattice constants depending on the Ni content were observed, suggesting that Ni enters the rutile structure of SnO$_2$ to some extent. No extra phases attributed to Ni were detected in the powders except for the sample synthesized from 20 : 80 [Ni(II)]/[Sn(II)], for which NiO as secondary phase was observed. The oxidation state and spatial distribution of Ni in the powders was investigated by X-ray photoelectron spectroscopy (XPS) and electron energy loss spectroscopy (EELS) measurements, respectively. For 6 at% and 9 at% Ni content, the presence of Ni^{2+} was established. The corresponding EELS mapping showed that a fraction of Ni (the one not forming part of the rutile phase) tended to accumulate at the pore edges, forming a nanometer-thick NiO layer. Compared to undoped SnO$_2$, Ni-containing powders exhibit a ferromagnetic response at low and room temperatures. Uncompensated spins at the surface of NiO are likely to contribute, in part, to the observed ferromagnetic properties.

Introduction

Both architecture and specific surface area are known to significantly impact the properties of materials. Indeed, exploiting the different pathways for which material architecture (or geometry) can be precisely controlled is one of the most attractive topics in materials science and, more recently, in nanoscale materials science. To date, many synthetic approaches have been devised and novel nanomaterials with different morphologies and structures have been prepared.[1,2] Among them, mesoporous materials (with pore sizes ranging from 2 nm to 50 nm) have captured wide attention due to the occurrence of internal connecting channels forming a network and their resulting large specific surface area. Thanks to their favourable architecture, mesoporous materials can show outstanding catalytic properties,[3–5] excellent optoelectronic effects,[6,7] visible fluorescence[8] and gas storage capabilities,[9] to name a few. Different methods such as sol–gel,[10,11] self-assembly,[12] dealloying,[13,14] and nanocasting[15]

are currently employed to obtain mesoporous products. Compared with other approaches, nanocasting is the preferred choice to prepare ordered mesoporous powders because the characteristics of the parent template, typically mesoporous silica or carbon, can be tailored on-demand by changing the type of precursor and its concentration, heat treatment temperature, and reaction time.[16] The morphology of the replica is determined to a great extent by the characteristics of the pre-fabricated template (pore topology, pore size, pore wall, and surface area).

Transition metal oxides are exciting materials with a wide range of technological uses in optoelectronic devices, superconductors, chemo-resistive gas sensors, and field emitting devices. Among metal oxides, tin dioxide (SnO$_2$), with a large band gap (E_g = 3.6 eV at 300 K), is an important n-type semiconductor. SnO$_2$ powders with mesoporous characteristics were firstly prepared by Ulagappan and Rao.[17] Since then, mesoporous SnO$_2$ has attracted significant attention because of its large specific surface area, thermal stability, and potential applications in different fields. Dimitrov *et al.* found that mesoporous SnO$_2$ prepared by sol–gel exhibited significant catalytic activity toward ethyl acetate oxidation and high selectivity towards CO$_2$.[18] Hossain *et al.* successfully synthesized mesoporous SnO$_2$ spheres, with different sizes, by electrochemical anodization followed by aging. The resulting SnO$_2$ spheres were applied in CdSe-sensitized solar cells as a photoanode

*Departament de Física, Facultat de Ciències, Universitat Autònoma de Barcelona, E-08193 Bellaterra, Barcelona, Spain. E-mail: Eva.Pellicer@uab.cat

*Institució Catalana de Recerca i Estudis Avançats (ICREA), Pg. Lluís Companys 23, E-08010 Barcelona, Spain

material.[19] According to Qi and co-workers, the large surface area and highly active surface of mesoporous SnO_2 nanospheres endowed effective binding of phosphopeptides.[20]

Doping oxide semiconductors with transition or noble metals can enhance the properties of these materials or even provide them with new functionalities. For instance, mesoporous Ag-doped SnO_2 synthesized by nanocasting from SBA-15 silica showed enhanced humidity sensing performance.[21] Likewise, transition metal-doped mesoporous CeO_2 nanoparticles exhibited enhanced catalytic activity for CO oxidation.[22] Recently, Co-, Fe- and Mn-doped In_2O_3 mesoporous powders have been reported to show room temperature ferromagnetic properties, hence constituting mesoporous oxide-diluted magnetic semiconductors (MODMS).[23] Actually, since the prediction of room-temperature ferromagnetic (RTFM) response in Mn-doped ZnO,[24] great efforts have been devoted toward the preparation of oxide-diluted magnetic semiconductors by doping wide band gap semiconductors with transition metal cations. Many groups have reported the occurrence of RTFM in nanowires,[25,26] thin films[27] and nanoparticles[28] by controllably doping semiconductor matrices made of TiO_2, ZnO, In_2O_3 and CaO with suitable transition metals. However, the occurrence of RTFM in MODMS has been very scarcely reported. The magnetic behavior of MODMS can be tuned by adjusting the transition metal doping level and the amount of oxygen vacancies.[23] Secondary phases (i.e., TM_xO_y where TM = transition metal) were actually found to also play a role on the magnetic properties, even though the secondary phases are typically antiferromagnetic (AFM) transition metal oxides. Nonetheless, AFM materials are encountering a renewed interest in spintronics, beyond their use in spin valves or tunnelling junction architectures, as essential elements in spin-transfer torque devices or encrypted magnetic memories.[29,30]

In this paper, the preparation of magnetically active mesoporous Ni-doped SnO_2 powders by means of nanocasting is presented. Notably, only Ag and Pd have been used as dopants in mesoporous SnO_2, and mostly for the purpose to improve its gas-sensing capabilities.[21,31] The replicas derived from KIT-6 silica show long-range order and feature low amounts of residual silicon. Different characterization methods have been used to investigate the morphology, crystallographic structure, and the oxidation state and distribution of Ni in the samples, namely by electron microscopies, X-ray diffraction (XRD) and X-ray photoelectron spectroscopy (XPS). The occurrence of ferromagnetism has been investigated by magnetometry. Interestingly,

appropriate doping of SnO_2 leads to an interesting ferromagnetic behaviour, both at low and room temperatures, whereas undoped SnO_2 does not show any ferromagnetic response regardless of the measuring temperature. For sufficiently high Ni doping level, the formation of a NiO nanocoating, surrounding the SnO_2 pore walls, is observed. By adjusting the thickness of this nanocoating, the ferromagnetic properties can be tailored. Larger saturation magnetization is observed for relatively thin NiO coatings, where the amount of surface uncompensated spins in NiO is maximized. This corresponds to intermediate Ni^{2+} doping concentration. For higher Ni^{2+} content, the thickness of the NiO coating increases and the saturation magnetization decreases, as the relative contribution of uncompensated spins to the ferromagnetic-like behaviour is reduced.

Experimental section

Synthesis of silica template

KIT-6 silica was chosen as the hard template to prepare mesoporous undoped and Ni-doped SnO_2. All the reagents were purchased from Sigma-Aldrich and used without further purification. In a typical synthesis, P-123 (6 g) was dissolved in a mixture of deionized water (220 g) acidified with 37 wt% HCl (12 g) by vigorous stirring (300 rpm) at 35 °C for 4 h. Then, 1-butanol (6 g) was added into the solution whilst stirring for another hour. Thereafter, 12.49 g of tetraethyl orthosilicate (TEOS) as the silicon source were added drop by drop into the solution and stirred for 24 h at the same temperature. The reaction vessel (sealed) was introduced in an oven at 80 °C for 24 h under static conditions. After the hydrothermal treatment, the resulting suspension was filtered and washed with deionized water several times. Finally, the collected powder was calcined in a tubular furnace at 550 °C under air flowing for 4 h.

Synthesis of undoped and Ni-doped mesoporous SnO_2

$SnCl_2 \cdot 2H_2O$ (stannous chloride dihydrate, Sigma-Aldrich 99.99%) was used as SnO_2 precursor. Firstly, KIT-6 silica (0.4 g), $SnCl_2 \cdot 2H_2O$ (0.6 g) and different amounts of $NiCl_2$ (nickel chloride, Sigma-Aldrich 99.99%) were finely ground in an agate mortar and pestle. The nominal [Ni(II)]/[Sn(II)] ratios used in the synthesis are listed in Table 1. The mixture was placed in a crucible and heated up to 85 °C inside a vacuum furnace (pressure < 10^{-4} mbar) to promote the infiltration of tin and nickel precursors within the KIT-6 silica host.[32,33] After 24 h, the samples were taken out and transferred into a tubular

Table 1 [Ni(II)]/[Sn(II)] molar ratio used in the synthesis, nominal Ni content in the resulting powers, corresponding actual percentages of Ni and Si detected by EDX, and crystallite size, microstrains and cell parameters of the SnO_2 phase

[Ni(II)]/[Sn(II)]	Ni nominal content (%)	Ni determined by EDX (%)	Si determined by EDX (%)	Crystallite size SnO_2 phase (nm) (±0.5)	Microstrains of SnO_2 phase (±1 × 10^{-5})	a (Å) of SnO_2 phase (±1 × 10^{-4})	c (Å) of SnO_2 phase (±1 × 10^{-4})
0 : 100	0	0	2	8.5	1.8 × 10^{-4}	4.7385	3.1885
5 : 95	2	1	4	8.1	3.5 × 10^{-3}	4.7397	3.1875
15 : 85	5	6	3	9.2	3.4 × 10^{-3}	4.7428	3.1854
20 : 80	7	9	3	10.6	3.7 × 10^{-3}	4.7416	3.1846

furnace for high temperature solid state reaction under air atmosphere. The temperature and heat treatment time were set at 700 °C and 2 h, respectively. Following the conversion of tin and nickel precursors, the silica template was selectively etched away using 1 M NaOH aqueous solution. Finally, sample powders were cleaned with deionized water and dried in oven.

Characterization of materials

Scanning and transmission electron microscopies (SEM and TEM, respectively) were used to investigate the morphology and microstructure of the powders. SEM observations were carried out on a Zeiss Merlin microscope operated at 3 keV whereas TEM analyses were performed on a Jeol-JEM 2011 operated at 200 kV. For the latter, the powders were dispersed in ethanol through sonication in an ultrasonic bath for 5 min. Then a few drops of the suspension were placed dropwise onto holey carbon TEM Cu grids. Electron energy loss spectroscopy (EELS) analyses were performed on a Tecnai F20 HRTEM/STEM microscope. Wide-angle X-ray diffraction (XRD patterns) were recorded on a PAN-alytical X'Pert Powder diffractometer equipped with Cu Kα radiation ($\lambda = 0.154$ nm) in the 20° to 80° 2θ range with step time of 0.78 s and step size of 0.026°. Rietveld refinements of the XRD full-patterns using the "Materials Analysis using Diffraction" (MAUD) software[34] were performed to extract the values of crystallite size, microstrains and lattice parameters as a function of Ni doping. The chemical composition and actual concentration of Ni in the doped SnO_2 powders were determined by energy dispersive X-ray spectroscopy (EDX) coupled to the SEM. Contents are given in at% throughout the manuscript and correspond to the averaging of minimum three independent measurements. XPS analyses (PHI 5500 Multitechnique System) were carried out with a mono-chromatic X-ray source (Kα Al line of 1486.6 eV energy and 350 W) under ultra-high vacuum (UHV), with pressure between 5×10^{-9} and 2×10^{-8} Torr, placed perpendicular to the analyser axis and calibrated using the $3d_{5/2}$ line of Ag with a full width at half maximum (FWHM) of 0.8 eV. The analysed area was a circle of 0.8 mm diameter for each sample. Peaks were charge corrected to adventitious C 1s set to 284.50 eV.[35] Experimental core-level spectra were fitted using Gaussian curves. Magnetic hysteresis loops were acquired on a superconducting quantum interference device (SQUID) at cryogenic (10 K) and room (300 K) temperatures.

Results and discussion

Morphology and crystallographic structure of undoped and Ni-doped SnO_2

Prior to the synthesis of the SnO_2-based replicas, the morphology of KIT-6 silica template was examined. A representative TEM
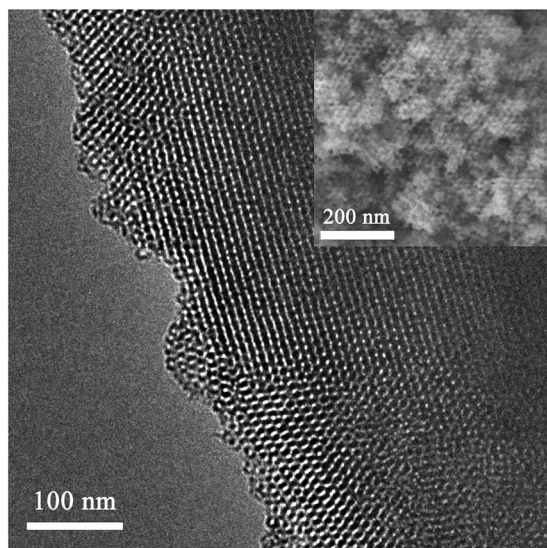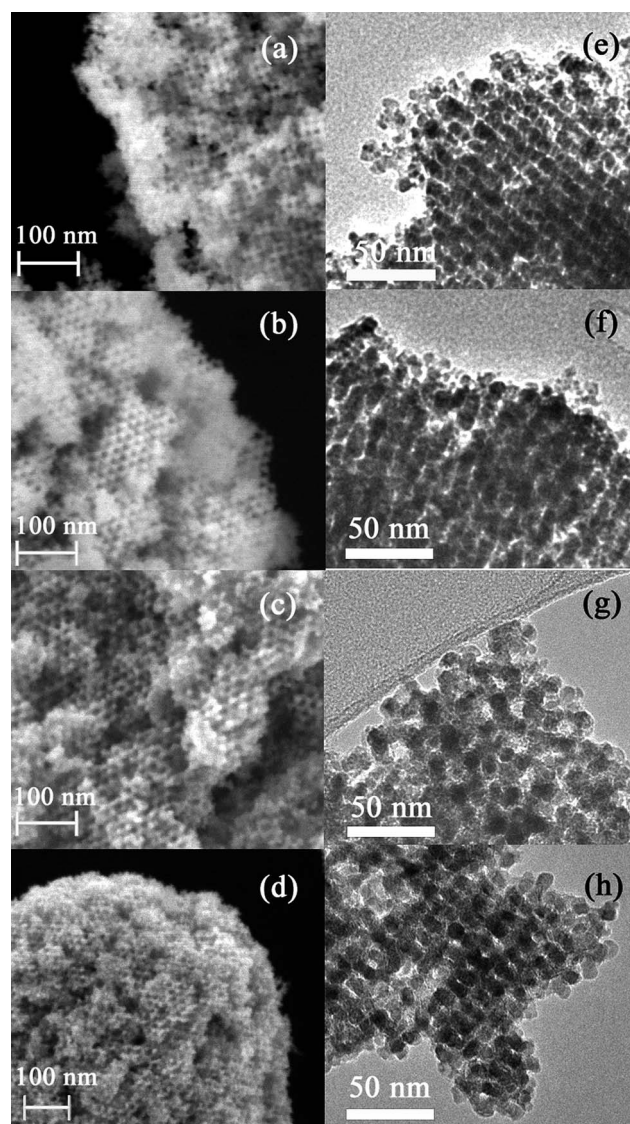

Fig. 2 Morphology of undoped and Ni-doped SnO_2 after KIT-6 silica template removal. (a) and (e), (b) and (f), (c) and (g), and (d) and (h) are the SEM and TEM images, respectively, of the powders obtained from different [Ni(II)]/[Sn(II)] molar ratios (0 : 100, 5 : 95, 15 : 85 and 20 : 80, respectively).

Fig. 1 TEM image of KIT-6 silica template. The inset shows an SEM image.

image of the bicontinuous cubic SiO_2 matrix is shown in Fig. 1. The quality of the template was judged as acceptable and pore size was estimated to be around 10 nm. The morphology of the derived SnO_2-based powders is depicted in Fig. 2. Both SEM (Fig. 2(a–d)) and TEM (Fig. 2(e–h)) images indicated that the powders exhibit an ordered arrangement of mesopores irrespective of the Ni loading. Indeed, the level of doping did not seemingly have a deleterious impact on the mesostructure of the SnO_2 replica. Relatively large ordered mesoporous domains were visible at the surface of the mesoporous particles by SEM.

Representative EDX patterns are shown for undoped and Ni-doped SnO_2 in Fig. 3a and b, respectively. The amounts of Ni and Si for all samples are listed in Table 1. For the doped powders, it was clear that Ni was successfully loaded into the SnO_2 matrix. The highest deviation (*ca.* 2%) between the nominal and actual Ni percentage was found for the sample with the highest dopant amount. Nevertheless, considering that the error in EDX measurements is about 1 at%, this is not a significant difference. Residual silicon content was kept below 4% in all cases. Probably the formation of strong Si–O–Sn bonds precludes a complete removal of the silica host, compared to other transition metal oxides. Si and Sn belong to IV-group elements; they possess the same number of outermost electrons and, in turn, similar chemical properties. In fact, SnO_2/SiO_2 composites can be simply obtained by solid–vapour reaction of mesoporous silica with tin vapour at 700 °C.[36] In this

work, authors detected Sn^{4+} bonded to the silica wall by bridged oxygen atoms. Nevertheless, our residual silicon amounts can be regarded as fairly low. This was possible through two consecutive cleaning steps of the $SiO_2@SnO_2$ composites with large volumes of NaOH solution to etch the silica template. Besides the formation of Si–O–Sn bonds, the presence of numerous nanochannels in the interior of the mesoporous particles likely hampers the effective dissolution of the silica host as the etching solution has to reach their inner space. Complementary XPS analyses indicated that although Si was present in all samples, its content was much lower than that determined by EDX. According to XPS analyses, the highest Si amount detected in the powders was 0.7%. Since XPS is a surface-sensitive technique, the detection of a larger amount of Si by EDX indeed suggests that the residual silicon is mainly concentrated in the inner cavities of the SnO_2 particles.

As shown in Fig. 4, all the samples are nanocrystalline. The main peak positions of the undoped and Ni-doped SnO_2 samples correspond to the rutile type tetragonal structure (JCPDS card no. 88-0287). No extra peaks are observed except for the sample produced from [Ni(II)]/[Sn(II)] of 20 : 80. In this case, additional diffraction peaks attributed to NiO are observed, which match those of JCPDS card no. 47-1049. Notice that these peaks are much narrower since a few big NiO particles had grown outside the mesoporous SnO_2 particles, as observed by TEM (not shown). Chaudhary and co-workers detected the
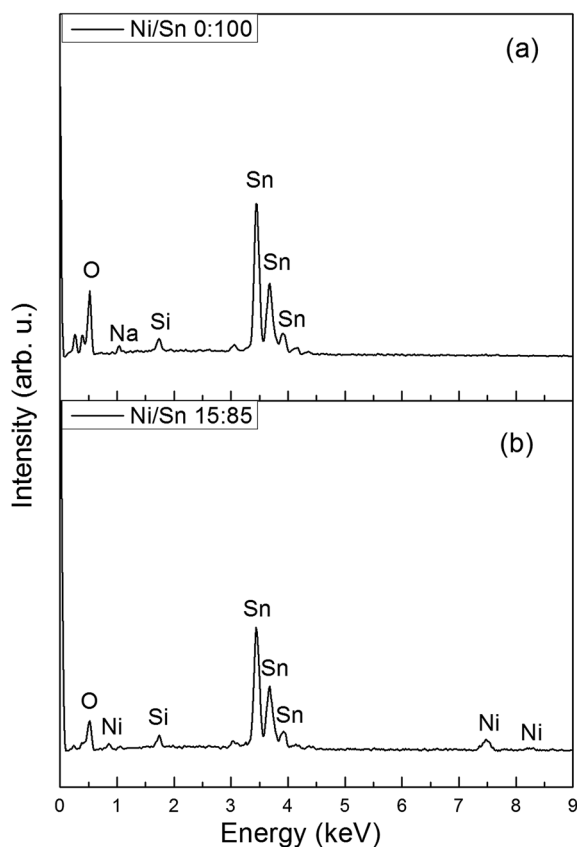

Fig. 3 EDX patterns of (a) undoped and (b) Ni-doped mesoporous SnO_2 obtained from [Ni(II)]/[Sn(II)] molar ratio of 15 : 85.

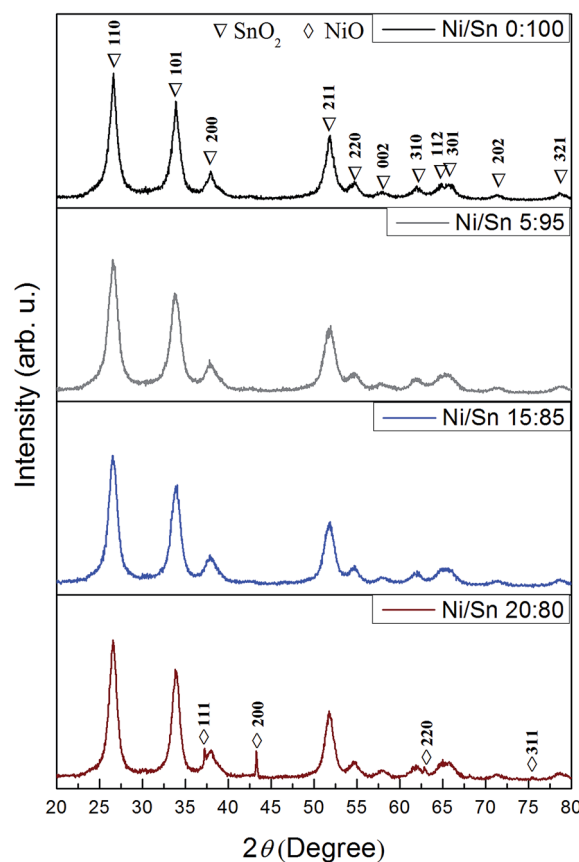**Fig. 4** XRD patterns of undoped and Ni-doped mesoporous SnO_2 obtained from varying [Ni(II)]/[Sn(II)] molar ratios.

formation of NiO in nanocrystalline thick SnO_2 films with Ni contents beyond 5%,[37] which is in agreement with our findings. The crystallite size of the SnO_2 phase, together with the microstrains and cell parameters, were calculated using MAUD. The calculated values are listed in Table 1. In broader strokes, both crystallite size and microstrains increased with the Ni doping although not in a monotonous manner. Crystallite size slightly decreased for the sample with the lowest Ni amount but increased thereafter. The level of microstrains rose significantly

when SnO_2 was doped with 1% and then remained fairly constant for higher loadings. The "*a*" and "*c*" lattice parameters increased and decreased, respectively, with the Ni doping level, in agreement with other works.[38] Fig. 5(a) is a HRTEM image of the 6%-doped SnO_2 powder. The SnO_2 skeleton consist of nanocrystals of about 5 nm in diameter, in agreement with XRD and other works in the literature.[39] The fast Fourier transform (FFT) of selected regions in the image shows spots whose interplanar distance matches tetragonal SnO_2. Selected area electron diffraction (SAED) analyses of the sample doped with higher Ni amount (9%) showed spots attributed to the NiO phase (Fig. 5(b)). In such a case, only the electron diffraction coming out from mesoporous particles was captured, avoiding the response of any big NiO crystal nearby.

In order to confirm the mesoporous long-range order of the samples, low-angle XRD analysis was carried out. Fig. 6 shows representative patterns of mesoporous KIT-6 silica, undoped SnO_2 and 6% Ni-doped SnO_2. The KIT-6 silica shows two well-resolved reflections attributable to (211) and (220) reflections. However, different from previous works,[32,40] the intensity of (211) peak is weaker than (220). After replication the peaks become inconspicuous, suggesting a partial loss of the long-range mesoporous order and concomitant decrease of the size of the ordered domains.

The samples with 6% and 9% Ni were subjected to XPS characterization to determine the oxidation state and the local chemical environment of the Ni element. At the same time, the effects induced by Ni to the SnO_2 matrix were investigated. Undoped SnO_2 was taken as the reference sample. Fig. 7(a) shows the XPS survey spectrum of the sample with 6% Ni. Sn 3d high resolution XPS spectra are displayed in Fig. 7(b). Upon Ni
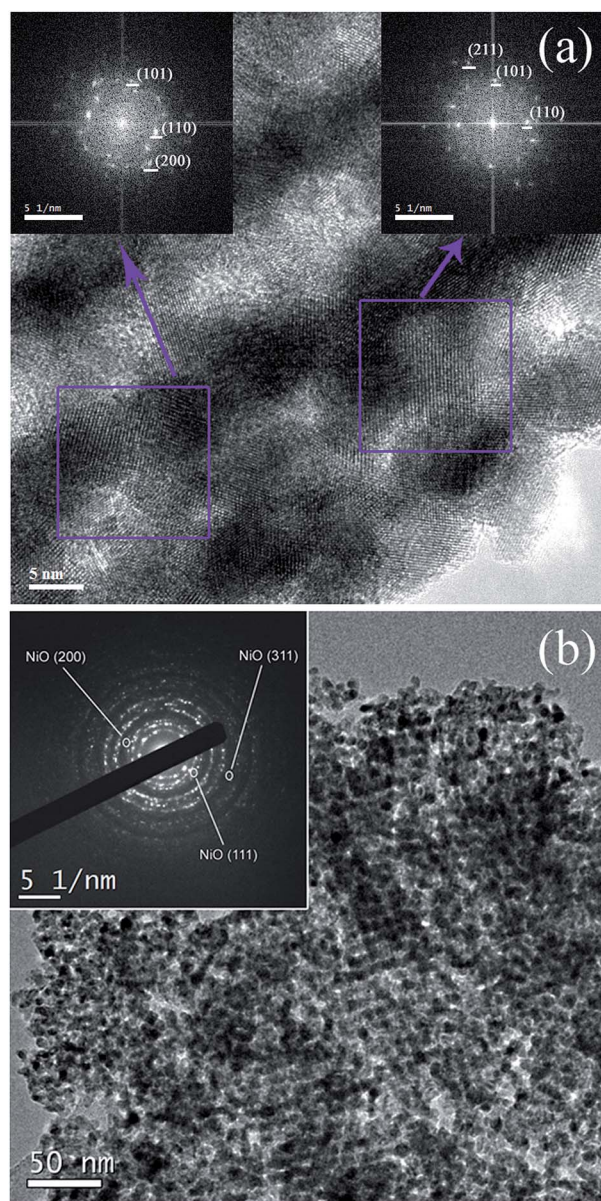

Fig. 5 (a) HRTEM image of the Ni-doped mesoporous SnO_2 powder synthesized from [Ni(II)]/[Sn(II)] molar ratio of 15 : 85. The insets show the FFT of the regions enclosed in the purple boxes. Underlined in white, some spots of the rutile-type tetragonal SnO_2 are indicated, along with the Miller indices of the corresponding crystallographic planes. (b) TEM image of the powder synthesized from [Ni(II)]/[Sn(II)] molar ratio of 20 : 80. The selected area electron diffraction pattern is shown in the inset. Circled spots can be unambiguously assigned to NiO phase.
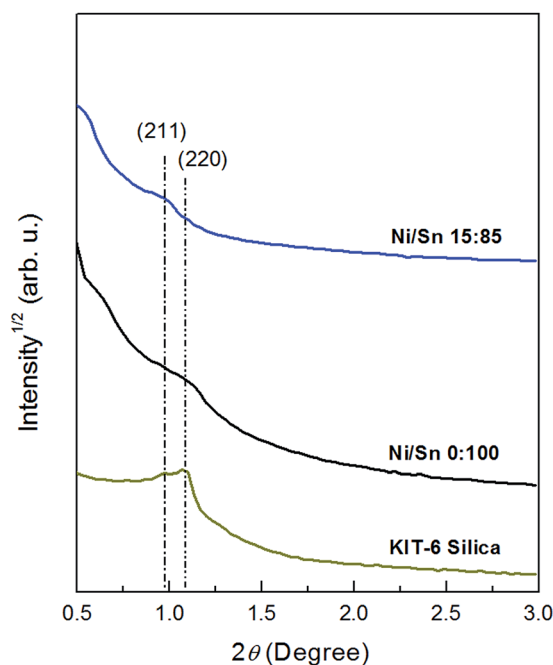

Fig. 6 Low-angle XRD patterns corresponding to KIT-6 silica template and mesoporous replicas obtained from [Ni(II)]/[Sn(II)] molar ratio 0 : 100 and 15 : 85.

doping, Sn 3d peaks shift toward lower binding energy compared with undoped SnO_2. It is conjectured that a larger number of oxygen vacancies and dangling bonds arise in the SnO_2 skeleton due to the introduction of Ni.[41] As a result, the relative number of electrons in the external electronic shell of Sn increases, which in turn causes a decrease of the binding energy of Sn compared to the undoped case.

The O 1s and Ni 2p XPS spectral windows of 6% Ni-doped SnO_2 are shown in Fig. 7(c) and (d), respectively. The O 1s spectrum can be deconvoluted into three main bands. The peaks at 530.51 eV and 529.41 eV correspond to the O 1s core level of the O^{2-} anions in the SnO_2 and NiO, respectively.[42–44] The peak at 532.07 eV is possibly attributed to chemisorbed oxygen at the defect sites of oxide crystal[45] or hydroxyl groups.[44]
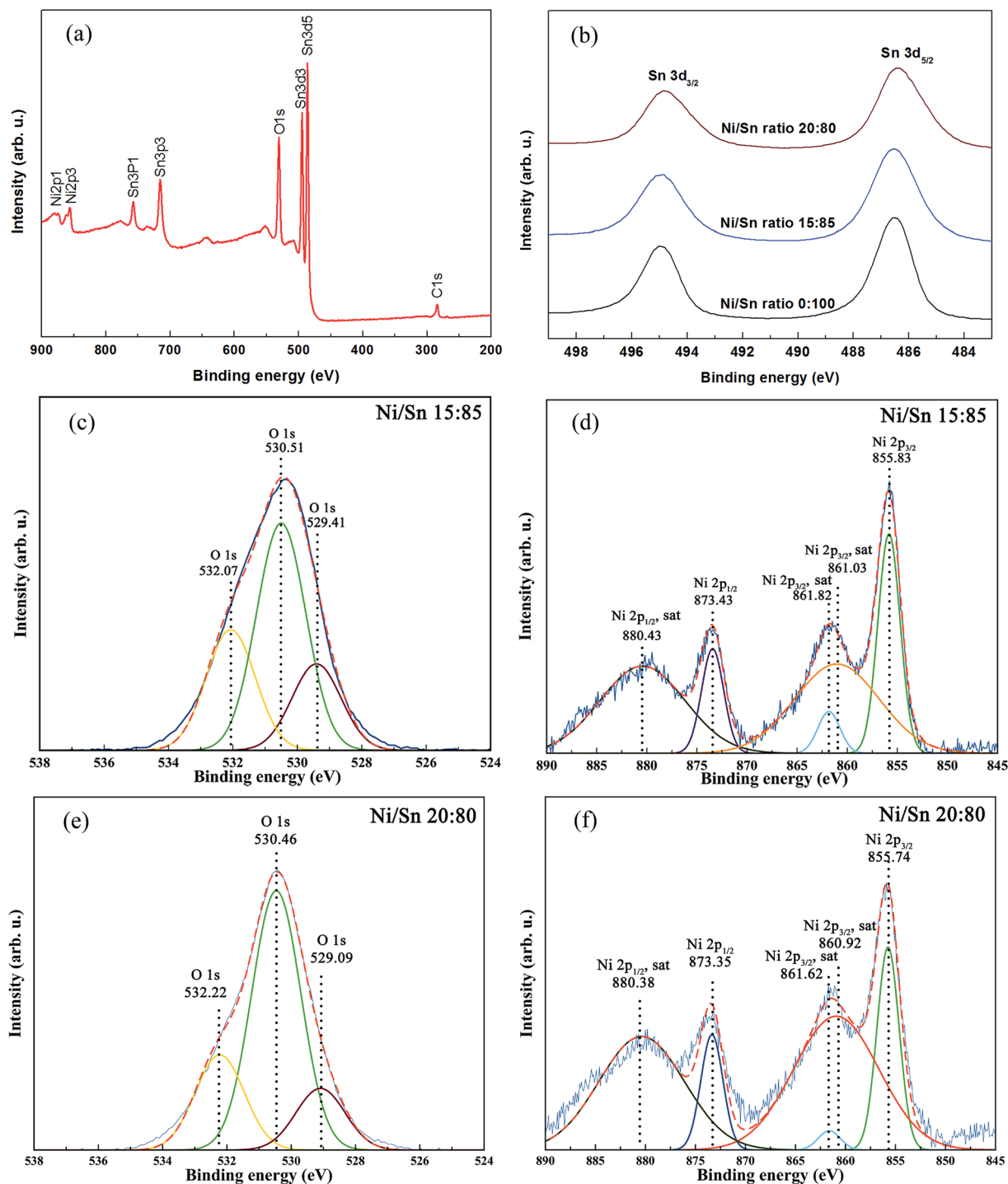

Fig. 7 (a) XPS survey spectrum of the powder obtained from [Ni(II)]/[Sn(II)] molar ratio of 15 : 85 (6% Ni). High resolution (b) Sn 3d for 15 : 85 (6% Ni) and 20 : 80 (9% Ni); (c) and (e) O 1s, and (d) and (f) Ni 2p for 15 : 85 (6% Ni) and 20 : 80 (9% Ni), respectively. In (b) the core-level Sn 3d spectrum of undoped SnO_2 is shown for comparison. 'Sat' denotes satellite peaks.

In Fig. 7(d), the separation distance between the peaks at 855.83 eV and 873.43 eV, which matches the binding energies expected for Ni $2p_{3/2}$ and Ni $2p_{1/2}$, is 17.60 eV. This difference is broader than the binding energy difference for metallic nickel, which is around 17.30 eV.[46] Furthermore, the position of the peaks exhibit some shift to higher binding energy compared with Ni^0.[47,48] This result excludes the occurrence of metallic Ni clusters in the 6% Ni-doped SnO_2. Based on the analysis, Ni ions possess a chemical valence of 2+. Experimental binding energies for Sn and O also indicate that their valences are 4+ and 2−, respectively. The O 1s and Ni 2p spectra for the sample with 9% Ni is very similar to that of 6% Ni (Fig. 7(e) and (f)), so the same reasoning applies.

EELS characterization

Taking into account the results previously obtained, the powder with 6% Ni (for which NiO phase was not detected in the XRD pattern but XPS data indicated it was definitely present) and that with 9% Ni (for which NiO as a secondary phase was clearly detected by XRD) were selected for EELS characterization. The goal was to investigate the spatial distribution of Ni in order to get further insight into the structural and magnetic characteristics of these two opposed samples. Fig. 8 shows the STEM and corresponding EELS mapping of a selected region for both cases. For the sample with the lower Ni content, Ni is detected mostly near the pore edges forming a kind of nanocoating, although red coloured

pixels superimposed to the green background are also observed at the inner region of the pore walls. For the sample with 9% Ni, a larger amount of Ni concentrated at the pore region was seemingly found. Orange coloured pixels result from the mixing of red (Ni) and green (O) colours. Nevertheless, the presence of big NiO particles outside the mesoporous particles should not be omitted in this case. When the amount of Ni largely exceeds the solubility limit, part of it can form the NiO skin around the pores but another fraction cannot be hosted and forms separate crystals outside. Although the coating surrounding the pores looks redder in the sample with 6% Ni, this does not mean it is made of metallic Ni. The pixels are not 100% red and indeed the L_3/L_2 ratio calculated from the EELS spectra taken at this region gives a value of 2.8 (see ESI, Fig. S1†), hence closer to NiO (for which the ratio is 3) than metallic Ni (for which the ratio is 1.5). This is in agreement with XPS analyses and, in fact, it makes sense considering that the conversion of precursors was carried out by heat-treatment in air.

In any case, the fact that NiO tends to accumulate at the pore/air interface makes the nanocasting route appealing toward ordered mesoporous nanocomposites. Actually, partial coating of mesoporous oxides has been reported in recent years by using successive impregnation and calcination procedures with different precursors.[49] Here, oxide semiconductor (SnO_2)/ antiferromagnetic (NiO) nanocomposites are obtained *in situ* in one-step nanocasting process.
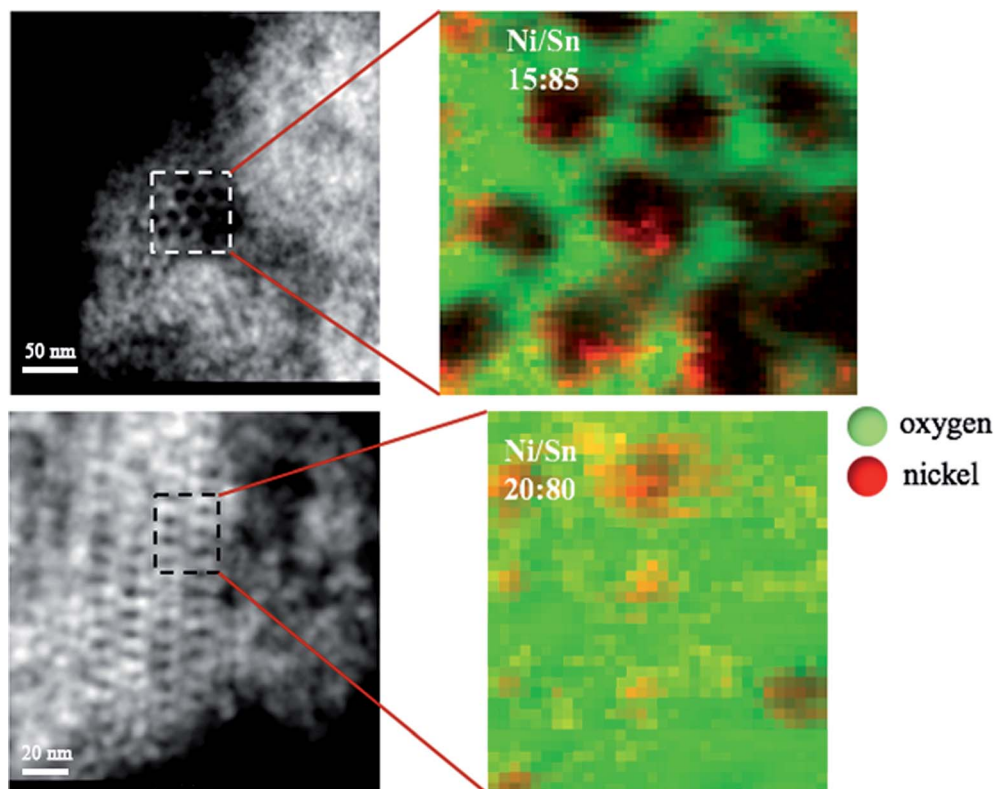

Fig. 8 STEM images and corresponding EELS mapping of the regions enclosed in the dashed squares for Ni-doped powders obtained from varying [Ni(ɪɪ)]/[Sn(ɪɪ)] molar ratios. Oxygen is in green while Ni is in red.

Magnetic properties of Ni-doped SnO₂ powders

The magnetic properties of the samples with varying Ni concentration were studied by acquiring hysteresis loops at 10 K and 300 K. The undoped SnO_2 exhibits inconspicuous paramagnetic behaviour at 10 K and typical diamagnetic behaviour at 300 K (Fig. 9). Meanwhile, the Ni-doped samples show a clear ferromagnetic signal at both temperatures although the saturation magnetization (M_S) does not scale with the Ni amount. The sample with 6% Ni possesses the largest M_S both at 10 K (5.88 emu g^{-1}) and 300 K (0.05 emu g^{-1}). A reduction of the M_S values is observed for the sample with 9 at% Ni. The ferromagnetic response observed in the Ni-containing powders is likely due to two contributions: (i) doping with the transition metal and concomitant formation of oxygen vacancies,[50] and (ii) uncompensated spins at the surface of the NiO nanocoating.[51,52] Notice that NiO is an antiferromagnet in bulk form, with a Néel temperature of 520 K.[53,54] However, it has been described that when the size of NiO decreases so that it falls well in the nanosize domain (e.g. nanoparticles), it might exhibit a ferromagnetic signal due to the presence of uncompensated spins at their surface. This would explain why M_S is higher in the sample with 6% than for 9% Ni. For the former, a larger amount of

uncompensated spins is expected from the very thin layer surrounding the SnO_2 pores. Meanwhile, for the latter, as the size of the NiO nanoparticles/nanoclusters has increased, the number of uncompensated spins decreases and so does the corresponding M_S.

Conclusions

In summary, we have successfully synthesized ordered mesoporous Ni-doped SnO_2 powders with tunable room-temperature ferromagnetic response as a function of the Ni loading. The optimum [Ni(II)]/[Sn(II)] molar ratio to guarantee the formation of a fully mesoporous product with the highest M_S is 15 : 85. This corresponds to a Ni content of 6%. At larger [Ni(II)]/[Sn(II)] molar ratio, the growth of a few NiO crystals outside the mesoporous structure could not be avoided. XRD analyses revealed that all samples possess the SnO_2 rutile structure irrespective of the Ni amount. Meanwhile, 2+ was the oxidation state of Ni, according to XPS data. Although dissolution of Ni ions in the SnO_2 lattice was proven by XRD, EELS analyses indicated that part of the dopant ions tended to accumulate at the pore edges. Hence, the observed room-temperature ferromagnetic response is attributed to both the Ni doping and the concomitant formation of oxygen vacancies, and to the occurrence of uncompensated spins at the surface of the NiO nanocoating. The present work demonstrates that by carefully controlling the doping level, ordered mesoporous semiconductor/antiferromagnetic nanocomposites can be obtained through one-step nanocasting process.
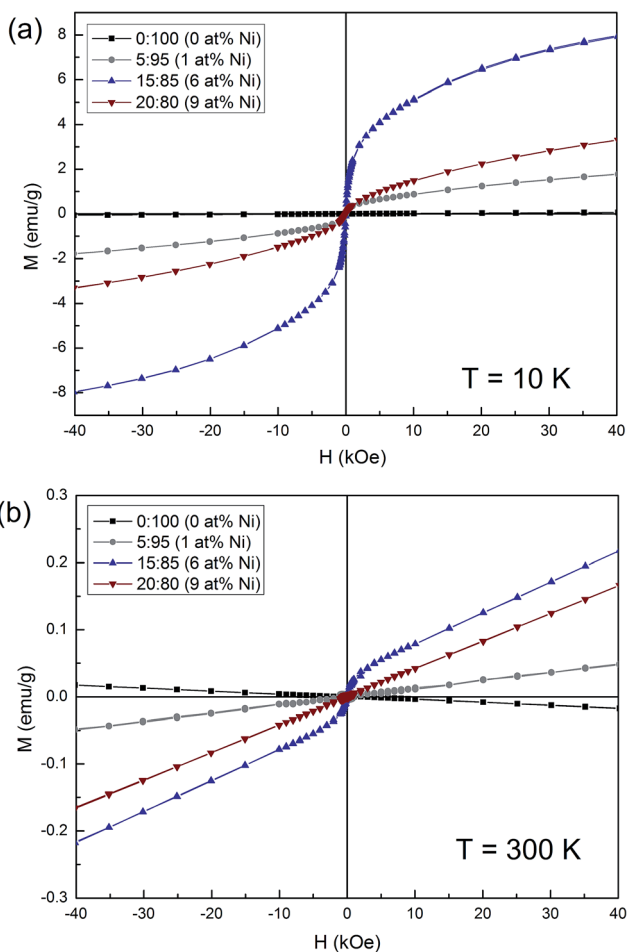
Fig. 9 Magnetic hysteresis loops of mesoporous undoped and Ni-doped SnO_2 powders obtained from varying [Ni(II)]/[Sn(II)] molar ratios (the corresponding experimental Ni percentages are in parentheses).

References

1 P. Chetri, P. Basyach and A. Choudhury, J. Solid State Chem., 2014, 220, 124–131.
2 C. T. Kresge and W. J. Roth, Chem. Soc. Rev., 2013, 42, 3663–3670.
3 L. Zhang and Y. Yin, Sens. Actuators, B, 2013, 185, 594–601.
4 E. Pellicer, E. Menéndez, J. Fornell, J. Nogués, A. Vantomme, K. Temst and J. Sort, J. Phys. Chem. C, 2013, 117, 17084–17091.
5 T. Grewe, X. Deng, C. Weidenthaler, F. Schüth and H. Tüysüz, Chem. Mater., 2013, 25, 4926–4935.
6 D. Chandra, S. Mridha, D. Basak and A. Bhaumik, Chem. Commun., 2009, 2384–2386.

7 E. J.   W. Crossland, N. Noel, V. Sivaram, T. Leijtens, J. A. Alexander-Webber and H. J. Snaith, *Nature*, 2013, **495**, 215–219.

8 M. Guerrero, S. Pané, B. J. Nelson, M. D. Baró, M. Roldán, J. Sort and E. Pellicer, *Nanoscale*, 2013, **5**, 12542–12550.

9 E. Kockrick, C. Schrage, L. Borchardt, N. Klein, M. Rose, I. Senkovska and S. Kaskel, *Carbon*, 2010, **48**, 1707–1717.

10 K. Niesz, P. Yang and G. A. Somorjai, *Chem. Commun.*, 2005, 1986–1987.

11 B. G. Trewyn, I. I. Slowing, S. Giri, H.-T. Chen and V. S.-Y. Lin, *Acc. Chem. Res.*, 2007, **40**, 846–853.

12 S. C. Warren, L. C. Messina, L. S. Slaughter, M. Kamperman, Q. Zhou, S. M. Gruner, F. J. DiSalvo and U. Wiesner, *Science*, 2008, **320**, 1748–1752.

13 J. Erlebacher, M. J. Aziz, a. Karma, N. Dimitrov and K. Sieradzki, *Nature*, 2001, **410**, 450–453.

14 Q. B. Zhang, A. P. Abbott and C. Yang, *Phys. Chem. Chem. Phys.*, 2015, **17**, 14702–14709.

15 A. H. Lu and F. Schüth, *Adv. Mater.*, 2006, **18**, 1793–1805.

16 Y. Jun, Y. Jung and J. Cheon, *J. Am. Chem. Soc.*, 2002, **124**, 615–619.

17 N. Ulagappan and C. N. R. Rao, *Chem. Commun.*, 1996, 1685–1686.

18 M. Dimitrov, T. Tsoncheva, S. Shao and R. Köhn, *Appl. Catal., B*, 2010, **94**, 158–165.

19 M. A. Hossain, G. Yang, M. Parameswaran, J. R. Jennings and Q. Wang, *J. Phys. Chem. C*, 2010, **114**, 21878–21884.

20 L. Li, S. Chen, L. Xu, Y. Bai, Z. Nie, H. Liu and L. Qi, *J. Mater. Chem. B*, 2014, **2**, 1121–1124.

21 V. K. Tomer and S. Duhan, *Sens. Actuators, B*, 2016, **223**, 750–760.

22 J. Zhang, J. Guo, W. Liu, S. Wang, A. Xie, X. Liu, J. Wang and Y. Yang, *Eur. J. Inorg. Chem.*, 2015, **2015**, 969–976.

23 E. Pellicer, M. Cabo, E. Rossinyol, P. Solsona, S. Suriñach, M. D. Baró and J. Sort, *Adv. Funct. Mater.*, 2013, **23**, 900–911.

24 T. Dietl, *Science*, 2000, **287**, 1019–1022.

25 S. A. Aravindh, U. Schwingenschloegl and I. S. Roqan, *J. Appl. Phys.*, 2014, **116**, 233906.

26 W. Wan, J. Huang, L. Zhu, L. Hu, Z. Wen, L. Sun and Z. Ye, *CrystEngComm*, 2013, **15**, 7887–7894.

27 J. Zhang, Q. Yun and Q. Wang, *Mod. Appl. Sci.*, 2010, **4**, 124–130.

28 B. Choudhury and A. Choudhury, *J. Appl. Phys.*, 2013, **114**, 203906.

29 A. H. MacDonald and M. Tsoi, *Philos. Trans. R. Soc., A*, 2011, **369**, 3098–3114.

30 T. Jungwirth, X. Marti, P. Wadley and J. Wunderlich, *Nat. Nanotechnol.*, 2016, **11**, 231–241.

31 J. Zhao, W. Wang, Y. Liu, J. Ma, X. Li, Y. Du and G. Lu, *Sens. Actuators, B*, 2011, **160**, 604–608.

32 J. K. Shon, S. S. Kong, Y. S. Kim, J. H. Lee, W. K. Park, S. C. Park and J. M. Kim, *Microporous Mesoporous Mater.*, 2009, **120**, 441–446.

33 E. Ramasamy and J. Lee, *J. Phys. Chem. C*, 2010, **114**, 22032–22037.

34 L. Lutterotti, S. Matthies and H.-R. Wenk, *IUCr Newsletter (International Union of Crystallography)*, 1999, **21**, 15.

35 H. Estrade-Szwarckopf and B. Rousseau, *J. Phys. Chem. Solids*, 1992, **53**, 419–436.

36 Z. C. Liu, H. R. Chen, W. M. Huang, J. L. Gu, W. B. Bu, Z. L. Hua and J. L. Shi, *Microporous Mesoporous Mater.*, 2006, **89**, 270–275.

37 D. K. Pandya, K. Gopinadhan, S. C. Kashyap and S. Chaudhary, *Synth. React. Inorg., Met.-Org., Nano-Met. Chem.*, 2008, **38**, 162–167.

38 P. P. Dorneanu, A. Airinei, M. Grigoras, N. Fifere, L. Sacarescu, N. Lupu and L. Stoleriu, *J. Alloys Compd.*, 2016, **668**, 65–72.

39 S. Lepoutre, J. H. Smått, C. Laberty, H. Amenitsch, D. Grosso and M. Lindén, *Microporous Mesoporous Mater.*, 2009, **123**, 185–192.

40 T. Waitz, B. Becker, T. Wagner, T. Sauerwald, C. D. Kohl and M. Tiemann, *Sens. Actuators, B*, 2010, **150**, 788–793.

41 D. L. Hou, H. J. Meng, L. Y. Jia, X. J. Ye, H. J. Zhou and X. L. Li, *Phys. Lett. A*, 2007, **364**, 318–322.

42 M. Kwoka, L. Ottaviano, M. Passacantando, S. Santucci, G. Czempik and J. Szuber, *Thin Solid Films*, 2005, **490**, 36–42.

43 A. Thøgersen, M. Rein, E. Monakhov, J. Mayandi and S. Diplas, *J. Appl. Phys.*, 2011, **109**, 113532.

44 B. P. Payne, M. C. Biesinger and N. S. McIntyre, *J. Electron Spectrosc. Relat. Phenom.*, 2009, **175**, 55–65.

45 I. S. Mulla, V. J. Rao, H. S. Soni, S. Badrinarayanan and A. P. B. Sinha, *Surf. Coat. Technol.*, 1987, **31**, 77–88.

46 A. D. Vogt, T. Han and T. P. Beebe, *Langmuir*, 1997, **13**, 3397–3403.

47 A. Lebugle, U. Axelsson, R. Nyholm and N. Mårtensson, *Phys. Scr.*, 1981, **23**, 825.

48 M. C. Biesinger, B. P. Payne, L. W. M. Lau, A. Gerson and R. S. C. Smart, *Surf. Interface Anal.*, 2009, **41**, 324–332.

49 E. Pellicer, M. Cabo, A. López-Ortega, M. Estrader, L. Yedra, S. Estradé, F. Peiró, Z. Saghi, P. Midgley, E. Rossinyol, I. V. Golosovsky, A. Mayoral, J. D. Prades, S. Suriñach, M. D. Baró, J. Sort and J. Nogués, *Nanoscale*, 2013, **5**, 5561–5567.

50 H. Wang, Y. Yan, X. Du, X. Liu, K. Li and H. Jin, *J. Appl. Phys.*, 2010, **107**, 103923.

51 R. Kodama, S. Makhlouf and A. Berkowitz, *Phys. Rev. Lett.*, 1997, **79**, 1393–1396.

52 P. Ravikumar, B. Kisan and A. Perumal, *AIP Adv.*, 2015, **5**, 87116.

53 J. C. Loudon, *Phys. Rev. Lett.*, 2012, **109**, 267204.

54 J. Stöhr, A. Scholl, T. Regan, S. Anders, J. Lüning, M. Scheinfein, H. Padmore and R. White, *Phys. Rev. Lett.*, 1999, **83**, 1862–1865.